



# Interaction of preferential evaporation and low-temperature chemistry in multicomponent counterflow spray flames

Matthew Bonanni\*, Matthias Ihme

*Department of Mechanical Engineering, Stanford University, Stanford, CA 94305, United States*

Received 6 January 2022; accepted 20 June 2022

Available online xxx

## Abstract

With transportation fuels being comprised of many compounds with different physicochemical properties, it is important to consider their impact on the combustion behavior. This study investigates the effects of preferential evaporation, in which different components of a liquid fuel evaporate at different rates, in the context of laminar counterflow spray flames. To isolate these effects, simulations are performed by considering a three-component Jet-A (POSF 4658) surrogate, consisting of *n*-dodecane, methylcyclohexane, and *m*-xylene with both preferential and non-preferential evaporation models. We show that the preferential evaporation of the more volatile cycloalkane in the preheated stream changes the gas-phase composition upstream of the flame. The lower reactivity of this component results in a downstream shift in the low-temperature chemistry zone. This leads to less penetration of the spray into the flame, a lower fuel consumption speed, and a higher gaseous mixture fraction throughout the reaction zones, compared to the non-preferential model. These effects highlight the necessity of considering preferential evaporation behavior when constructing models for multicomponent spray combustion.

© 2022 The Combustion Institute. Published by Elsevier Inc. All rights reserved.

**Keywords:** Spray combustion; Preferential evaporation; Low-temperature chemistry; Counterflow spray flame

## 1. Introduction

Many propulsion systems rely on liquid propellants, thanks to their high energy density and ease of storage and handling [1]. These fuels are burned in a process of atomization and subsequent spray combustion. Spray combustion is a com-

plex phenomenon that requires the consideration of multiple physical and chemical processes, including spray breakup, evaporation, mixing, and combustion [2–4]. Improved fundamental understanding of this process enables more advanced numerical simulation techniques [5–8] which, in turn, enable the development of more reliable and efficient combustors, as well as the utilization of sustainable aviation fuels.

While much effort has been dedicated to the study of combustion of large hydrocarbon fuels [9,10] and spray flames with single-component fuels

\* Corresponding author.

E-mail address: [mbonanni@stanford.edu](mailto:mbonanni@stanford.edu) (M. Bonanni).

[3,5,11,12], practical transportation fuels consist of a large number of components [1]. These individual components have different phase-change and chemical properties. In a spray combustion context, this leads to an evaporation process in which the droplet composition changes throughout the combustion process, depositing different fuel components into different regions of the domain. Additionally, these different components exhibit a varying combustion behavior. Important properties such as their ignition delay time may vary widely, especially across low-temperature and high-temperature combustion regimes. In particular, low-temperature chemistry has a significant impact on the structure of spray flames [13]. Even in single-component spray flames, evaporation largely dominates other processes in determining the flame structure [14]. All of these features indicate a significant dependence of the spray flame structure on the preferential evaporation process; yet, this has not been fully investigated and predictive models have not yet been developed.

Prior work has explored the vaporization and ignition of multicomponent fuel sprays, including studies dedicated to the development of models for preferential evaporation [15–18]. Studies examining effects of preferential evaporation have shown that for conditions where evaporation and chemical time scales are similar, the ignition time considering preferential evaporation deviates significantly from the constant fuel composition (non-preferential) model [19]. Additionally, it has been demonstrated in these homogeneous mixtures that turbulence enhances fuel vaporization and couples with preferential evaporation to yield fundamentally different ignition behaviors [20]. Evaporation effects have also been studied in counterflow spray flames [21], showing that finite evaporation rates impact both pre-flame pyrolysis and peak temperature compared to prevaporized conditions. In a free flame configuration, Shastry et al. [22] demonstrated that more volatile compounds increase the effective equivalence ratio and less volatile compounds led to a secondary diffusion flame.

To date, however, the impact of preferential evaporation behavior on spray flame structure and characteristics has not been explored across a wide range of operating conditions [13]. Therefore, the objective of this work is to determine the significance of these effects. This work considers a counterflow spray flame configuration, as depicted in Fig. 1. This configuration enables access to a wide range of operating conditions at steady state, and allows for the relevant conditions to be examined parametrically [12,23]. With this configuration, the present work seeks to isolate preferential evaporation effects by characterizing the differences in properties between non-preferentially evaporating (corresponding to the *diffusion limit* described in Govindaraju et al. [20], Sirignano [24]) and preferentially evaporating (approaching the *distillation*

*limit* [20,24]) liquid spray flames, as well as to determine the underlying causes of these differences. These effects are explored across operating conditions, including equivalence ratio and droplet diameter, to determine the impact of preferential evaporation on the spray flame structure.

The remainder of this paper has the following structure: Section 2 presents the model formulation, including governing equations for both gas and liquid phases, models for inter-phase exchange, and solution methods. Section 3 details the properties of the Jet-A surrogate fuel used in this study, examining these through numerical measurements and zero-dimensional droplet simulations. Section 4 presents simulation results. A parametric study is performed, and the results are investigated by analyzing the flame structure. Section 5 closes the paper by summarizing the findings of this study and offering conclusions.

## 2. Methodology

### 2.1. Governing equations

The present work considers an axisymmetric counterflow spray flame as described in Darabiha et al. [12] and Franzelli et al. [25] and depicted in Fig. 1. In this configuration, a stream of air mixed with fuel spray (1) injected on one side opposes a stream of pure air (2). Both inlets and phases share the same axial velocity  $v_g^{(1)} = v_l^{(1)} = -v_g^{(2)}$ , where superscripts (1) and (2) denote the fuel and oxidizer inlets and subscripts  $g$  and  $l$  denote the gaseous and liquid phases, respectively, and all have zero radial velocity at the inlets ( $U_g^{(1)} = U_l^{(1)} = U_g^{(2)} = 0$ ). At each inlet, the gas phase is preheated, having equal temperature  $T_g^{(1)} = T_g^{(2)}$ , while the liquid temperature is  $T_l^{(1)} = 300$  K.

The assumption of a constant pressure gradient in the radial direction  $\frac{1}{r} \frac{\partial p}{\partial r} = -J$ , where  $r$  is the

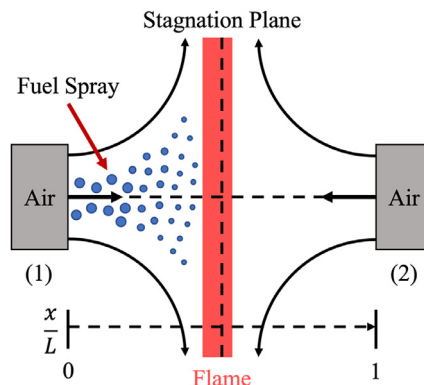


Fig. 1. Schematic representation of the counterflow spray flame configuration.

radial coordinate, enables a similarity analysis in which all properties of the spray and gas phases depend only on the axial coordinate  $x$  [11]. For the gas phase, the resulting governing equations for mass, radial and axial momentum, energy, and species, as extended from Darabiha et al. [12], take the following form:

$$2\rho_g U_g + \frac{\partial \rho_g v_g}{\partial x} = n_l \dot{m}_l, \quad (1a)$$

$$\rho_g U_g^2 + \rho_g v_g \frac{\partial U_g}{\partial x} = \frac{\partial}{\partial x} \left( \mu_g \frac{\partial U_g}{\partial x} \right) + J + n_l \dot{m}_l (U_l - U_g) - n_l \frac{f_r}{r}, \quad (1b)$$

$$\rho_g v_g c_{p_g} \frac{\partial T_g}{\partial x} = \frac{\partial}{\partial x} \left( \lambda_g \frac{\partial T_g}{\partial x} \right) - \sum_{k=1}^K h_k W_k \dot{\Omega}_k - \left( \sum_{k=1}^K \rho_g Y_{g,k} V_k c_{p_{gk}} \right) \frac{\partial T_g}{\partial x} + n_l \dot{m}_l c_{p_{gF}} (T_l - T_g) - n_l \dot{m}_l q, \quad (1c)$$

$$\rho_g v_g \frac{\partial Y_{g,k}}{\partial x} = - \frac{\partial}{\partial x} (\rho_g Y_{g,k} V_k) + W_k \dot{\Omega}_k + n_l \dot{m}_l (\varepsilon_k - Y_{g,k}), \quad (1d)$$

where  $\rho$  is the density,  $n_l$  is the droplet number density,  $\dot{m}_l$  is the mass evaporation rate of a single droplet,  $\mu$  is the viscosity, and  $f_i$  is the component of the droplet drag force in the  $i$ th direction, modeled with Stokes' law [26], and  $c_p$  is the constant-pressure heat capacity, with subscripts  $k$  indicating a property of the  $k$ th species and  $F$  indicating a mixture average for the fuel.  $h$  is the specific enthalpy,  $W$  is the molar mass, and  $\dot{\Omega}$  is the molar production rate due to chemistry;  $V_k$  is the diffusion velocity of species  $k$ , modeled with Fick's law and a mixture-averaged diffusion coefficient;  $q$  is the rate of heat transfer from the gas to a single droplet,  $Y_k$  is the mass fraction of species  $k$ , and  $\varepsilon$  is the evaporation rate fraction, detailed below in Section 2.2.

The liquid phase is also treated in an Eulerian manner [12], under the assumption of a dilute spray. Based on the similarity analysis [11], the liquid phase equations for droplet mass  $m_l$ , radial and axial velocity  $U_l$  and  $v_l$ , temperature  $T_l$ , and species mass fraction  $Y_{l,k}$  can be written as extended from Darabiha et al. [12] as:

$$v_l \frac{\partial m_l}{\partial x} = -\dot{m}_l, \quad (2a)$$

$$m_l U_l^2 + m_l v_l \frac{\partial U_l}{\partial x} = \frac{f_r}{r}, \quad (2b)$$

$$m_l v_l \frac{\partial v_l}{\partial x} = f_x, \quad (2c)$$

$$m_l c_{p_l} v_l \frac{\partial T_l}{\partial x} = \dot{m}_l (q - L_v), \quad (2d)$$

$$\frac{\partial}{\partial x} (Y_{l,k} v_l) + 2 Y_{l,k} U_l = - \frac{\dot{m}}{m_l} (\varepsilon_k - Y_{l,k}), \quad (2e)$$

$$2 n_l U_l + \frac{\partial n_l v_l}{\partial x} = 0, \quad (2f)$$

where  $m_l$  is the mass of a single droplet and  $L_v$  is the latent heat of vaporization.

Flames will be characterized in terms of the nominal equivalence ratio  $\phi$  as well as the initial droplet diameter  $d_d^{(1)}$ . Here, we define

$$\phi = \frac{32(m + \frac{n}{4})}{12m + n} \frac{Y_F^{(1)}}{Y_O^{(1)}} \quad (3)$$

where  $m$  and  $n$  are respectively the carbon and hydrogen numbers of the arbitrary hydrocarbon fuel  $C_m H_n$  (effective carbon and hydrogen numbers are used for multicomponent fuels), and  $Y_F^{(1)}$  and  $Y_O^{(1)}$  are the fuel and oxygen mass fractions in the fuel-air stream ( $Y_F^{(1)}$  is computed as if the droplets were fully prevaporized).

## 2.2. Preferential evaporation

The formulation described in Franzelli et al. [25] has been extended, as in Kitano et al. [17] and Wang et al. [21], to incorporate multicomponent fuels with preferential evaporation. A thin-film assumption is made in which a boundary layer of saturated, vaporized fuel surrounds the droplet, and the droplet is assumed to have spatially uniform composition in the slow-vaporization limit [16,18]. In this formulation, the overall droplet evaporation rate is computed as  $\dot{m}_l = 2\pi d_d \rho_g \bar{D}_g \ln(1 + B_M)$ , where  $d_d$  is the droplet diameter,  $\bar{D}_g$  is the mixture-averaged diffusion coefficient of the fuel vapor, and  $B_M$  is the Spalding mass-transfer number. The evaporation rate of each species,  $\dot{m}_{l,k} = \varepsilon_k \dot{m}_l$ , is determined by its evaporation fraction,  $\varepsilon_k$ , defined as Miyagawa et al. [15]:

$$\varepsilon_k = \frac{Y_{g,k} - Y_{s,k}(1 + B_M)^{\alpha_k}}{1 - (1 + B_M)^{\alpha_k}} \quad (4)$$

where  $Y_{s,k}$  denotes the mass fraction of the  $k$ th species at the surface of the droplet. This is determined from the species mole fraction  $X_{s,k} = X_{l,k} p_{sat,k}/p$ , based on the saturation pressure  $p_{sat}$ . This model allows the droplet composition to change over time as the components preferentially evaporate. If instead the diffusion limit [18,24] is considered, the assumption is made that  $\varepsilon_k = Y_{l,k}$ . This yields a mixture-averaged non-preferential

formulation in which the droplet composition remains constant. Throughout this study, since the spray and gas enter the domain at the same velocity, the slip velocity remains low, with a typical droplet Reynolds number on the order of  $10^{-2}$ . As a result, the boundary layer on the droplet and other convective effects such as internal transport, which would suppress preferential evaporation due to enhanced mixing, are insignificant [27].

Eqs. (1) and (2) are solved using a pseudo-time stepping method in which a temporal term is added to each equation. The gas and liquid phases are independently advanced in time until the system is converged such that attempts to solve the system with a Newton–Raphson method are successful. The solver is implemented as an extension of the one-dimensional gas flame solver of Cantera [28].

### 3. Surrogate fuel composition

Since this investigation is motivated by application to aviation fuels, we consider the combustion of a Jet-A (POSF 4658) surrogate. This surrogate, with comparable liquid-phase, phase change, and combustion properties, was developed by Narayanaswamy et al. [29], composed of 30.3% *n*-dodecane, 48.5% methylcyclohexane (MCH), and 21.2% *m*-xylene by mole. Liquid phase thermodynamic properties and phase change properties are gathered from the NIST Chemistry WebBook [30].

It is insightful to consider the evaporation process of a droplet in a zero-dimensional, non-reacting setting, in order to compare the droplet evaporation times for the preferential and non-preferential evaporation cases. To this end, we simulate a stationary  $50\text{ }\mu\text{m}$  fuel droplet at 300 K in air at 800 K and 1 atm, which is representative of the injection conditions of our one-dimensional simulations in Section 4. The results are presented in Fig. 2. Here, we note the changing composition of the droplet in the preferential case, while the non-preferential case maintains a constant composition. Early in the evaporation process, while the composition of the evaporating vapor is different in the two cases, the liquid composition is nearly identical. The vapor-phase properties of the components in this surrogate, such as density and diffusion constant, are very close in value, such that changes in the vapor composition do not greatly affect the overall evaporation rate. Therefore, the evaporation rate is initially very similar. Eventually, however, mass evaporation rates diverge due to the change in the Spalding mass transfer number, which is driven by the change in total fuel mass fraction at the surface of the droplet, which is in turn driven by the change in the liquid-phase composition. Additionally, the droplet with non-preferential evaporation plateaus at a lower liquid temperature of approximately 350 K, while the preferentially-evaporating droplet continues to in-

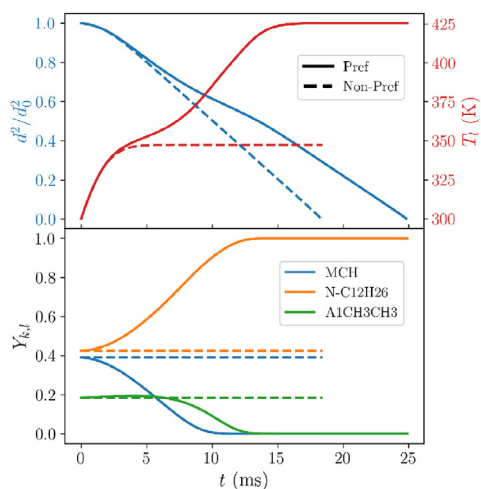


Fig. 2. Simulations of surrogate fuel droplet evaporation with  $d_0 = 50\text{ }\mu\text{m}$ ,  $T_{l,0} = 300\text{ K}$  in 800 K air, for both preferential and non-preferential evaporation models.

crease in temperature to approximately 425 K. This behavior is related to the boiling temperatures of the components, which are 489.0 K, 374.0 K, and 412.3 K for *n*-dodecane, MCH, and *m*-xylene, respectively. Most significantly, we note that the preferentially evaporating droplet has an evaporation time which is 35% longer than the droplet with non-preferential evaporation. In the preferential case, the most volatile component, MCH, evaporates, followed by *m*-xylene, leaving a nearly pure *n*-dodecane droplet, which takes longer to evaporate as this is the least volatile component.

The publication of Narayanaswamy et al. [29] also includes a corresponding detailed chemical mechanism for the surrogate, from which Fang et al. [31] developed a skeletal mechanism with 110 species and 352 reactions, which we use in the present work. This skeletal mechanism includes semi-global low-temperature chemistry (LTC) sub-mechanisms for MCH and *n*-dodecane, which is critical to the counterflow spray flame behavior [13]. As described by Curran [32], in this low-temperature regime, alkanes undergo hydrogen abstraction, yielding alkyl (R) radicals which react with oxygen to form alkylperoxy (ROO) radicals. At low temperatures, these ROO radicals isomerize into hydroperoxyalkyl (QOOH) radicals at a greater rate than they decompose into smaller alkenes and hydroxyl radicals, with the latter process being responsible for the non-monotonic reactivity at intermediate temperatures. This non-monotonic reactivity is evident in the ignition delay time, depicted in Fig. 3.

Fig. 3 shows that *n*-dodecane is the most reactive component in the LTC region, followed by MCH and then by *m*-xylene, for which an LTC sub-mechanism is not included due to its low reactiv-

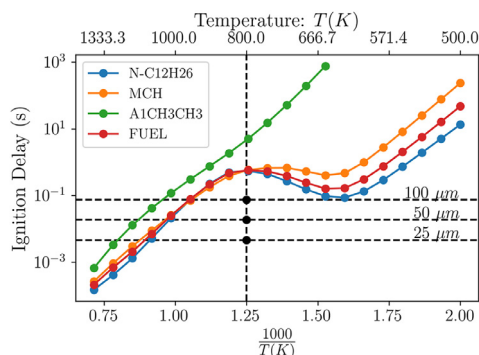


Fig. 3. Ignition delay times of the 3-component surrogate and its individual components, computed with the Fang mechanism at  $\phi = 1.0$ . Preferential evaporation times of 25, 50, and 100  $\mu\text{m}$  droplets in 800 K air are indicated with dashed lines.

ity. By isolating the heat release due to these LTC submechanisms and comparing this to the overall heat release, we can better characterize the LTC regions in the forthcoming analysis. Fig. 3 also includes the droplet evaporation times for 25, 50, and 100  $\mu\text{m}$  droplets in 800 K air using the preferential model under the conditions described above. With the preferential model yielding longer evaporation times as shown above, we note that in the low-temperature regime, even for the largest droplet diameter of 100  $\mu\text{m}$ , the ignition delay times of this fuel are greater than the evaporation times. This implies a separation of these physical processes in the conditions considered by this study.

#### 4. Results

In the present study, we consider a monodisperse surrogate fuel spray, injected at a temperature  $T_i^{(1)} = 300$  K in a stream of air. The inlet gas temperature  $T_g^{(1)} = T_g^{(2)} = 800$  K. The injection axial velocity,  $v_i$ , is 2 m/s, and the inlets are separated by a distance of  $L = 8$  cm. The nominal system pressure is 1 atm. Equivalence ratios between 1.5 and 3.0 and droplet diameters between 28 and 100  $\mu\text{m}$  are considered. The choice of the droplet diameter was motivated from experimental data, showing that for spray flames of *n*-dodecane and other liquid fuels the measured Sauter mean diameters approximately span the 30–100  $\mu\text{m}$  range [33], with 100  $\mu\text{m}$  being on the larger side for aviation gas-turbines. Additionally, we sought to span an order of magnitude change in this parameter, as well as capture the minimum size at which droplets stopped penetrating the flame. The equivalence ratio bounds were selected to span a range at which the different flame structures identified by Xie et al. [13] were represented in the parameter space.

Fig. 4 presents a selection of three flamelet results for conditions which span the range considered in this study. Representing the richest cases considered, with the largest droplet diameters, the resulting flame solutions for  $\phi = 2.91$ ,  $d_d^{(1)} = 100$   $\mu\text{m}$  are depicted in Fig. 4a. These plots are presented in physical space, with spray-air injection at  $x/L = 0$  and pure air injection at  $x/L = 1$ . Here, we can see that the flames for both preferential and non-preferential cases have taken on a collocated flame structure in which the partially-premixed and diffusion reaction zones are very near to each other [13]. Defining the boundary of the reaction region on the fuel stream side as the location of the initial temperature rise, we see that in both cases, the spray significantly penetrates the flame, even into the high-temperature reaction zone, due to the large droplet diameter. The effect of preferential evaporation on the gas-phase composition is also evident. In the non-preferential case, gas-phase mass fractions of all liquid fuel components increase proportionally as the spray evaporates. In the preferential case, however, there is significantly more MCH due to its high volatility, while nearly no *n*-dodecane evaporates until the spray has penetrated the flame, and this *n*-dodecane is consumed as it evaporates, resulting in a low mass fraction even in this region. We may also note the presence of the LTC region in both cases, in which the LTC heat release comprises the majority of the overall heat release. As will be discussed in detail in Section 4.1, this region occurs further downstream in the preferential case.

The intermediate case with  $\phi = 2.36$ ,  $d_d^{(1)} = 50$   $\mu\text{m}$ , depicted in Fig. 4b, exhibits a flame structure which has broadened, with the partially-premixed and diffusion reaction zones growing increasingly separated. Here, due to the smaller droplet diameter, the spray is nearly fully evaporated before it reaches the reaction zones, but it does penetrate the LTC zone. In the preferential case, we see that the MCH evaporates quickly, followed by *m*-xylene, leaving nearly pure *n*-dodecane droplets which eventually evaporate. Interestingly, while the heat release rates of the flames seem to agree very well in the high-temperature regions, the LTC zone occurs significantly further downstream with respect to the injector in the preferential case, leading to significantly less spray penetration despite the longer droplet lifetime. The presence of MCH far upstream in the preferential flame is insufficient to trigger the LTC and this reaction zone does not occur until more *n*-dodecane has vaporized.

Finally, we consider the lowest equivalence ratio, smallest diameter case with  $\phi = 1.58$ ,  $d_d^{(1)} = 28$   $\mu\text{m}$  in Fig. 4c. Here, as expected for these conditions, the flame has taken a distributed structure [13]: there is still a low-temperature chemistry zone, but the high-temperature chemistry extends across separate partially-premixed and dif-



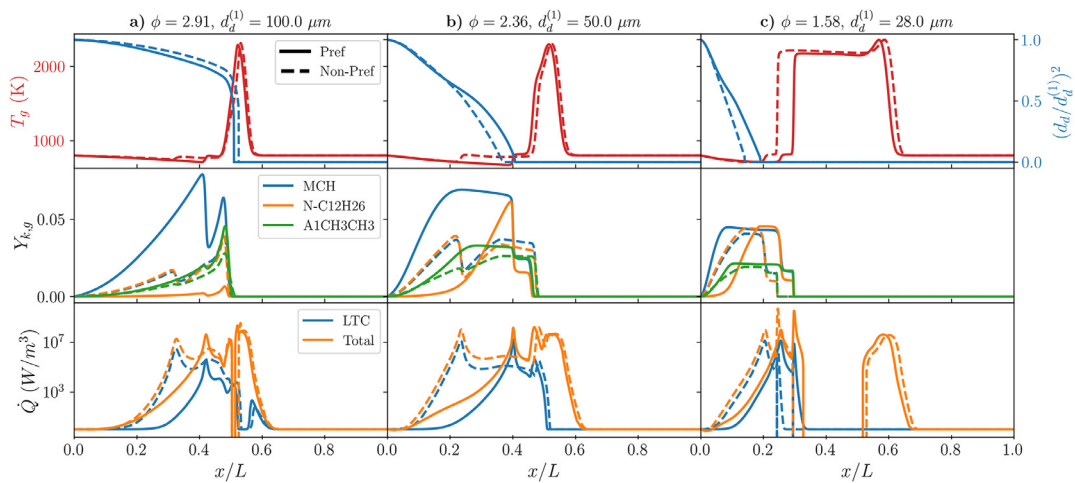


Fig. 4. Jet-A surrogate spray flame structure for varying equivalence ratio and injected droplet diameter. Plots of droplet diameter are normalized by the diameter at injection,  $d_d^{(1)}$ . Preferentially evaporating spray flames are indicated with solid lines, while non-preferential flames are indicated with dashed lines.

fusion zones. The partially premixed zone appears to have some LTC behavior, but this is overshadowed by the HTC. In this regime, both the LTC and partially-premixed zones have shifted downstream in the preferential case. Neither spray penetrates the flame, because at this small droplet diameter, the evaporation time is very short, as shown in Section 3.

#### 4.1. Variation of equivalence ratio and droplet diameter

Within the bounds of droplet diameter and equivalence ratio depicted above, we may begin to make comparisons of flame behavior across operating conditions by defining global quantities describing each flame. In particular, we define the bounds of the reaction region as the locations where the gas temperature rises 10 K above its minimum on either side of the stagnation plane. The first global metric that we will consider is the droplet *penetration distance*, defined as the distance between the initial temperature rise of the flame and the spray cutoff point (where the droplet diameter becomes negligibly small). This is a valuable metric because, as we will explore further below, large droplet penetration is associated with a change in the gas-phase composition for preferential flames. An ensemble of flame simulations with varying  $\phi$  and  $d_d^{(1)}$  is performed for both preferential and non-preferential evaporation models, and the results are presented in Fig. 5.

Here, we can see that the penetration distance increases for both models with droplet diameter, and this effect is slightly more pronounced at higher equivalence ratios. Despite the longer droplet lifetimes, however, the penetration distance of the pref-

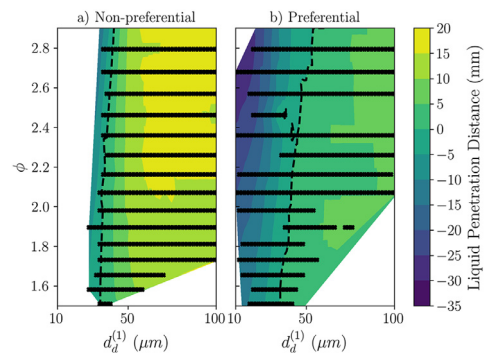


Fig. 5. Comparison of penetration distance across varying  $\phi$  and  $d_d^{(1)}$  for (a) non-preferential and (b) preferential flames. The contour of zero penetration distance is indicated by a dashed line. Solution conditions are indicated with black symbols.

erential flames is consistently lower. Even the preferential flames with the largest droplet diameters penetrate less than some of the non-preferential flames with the smallest diameters. Additionally, for the same equivalence ratio, a larger diameter droplet is necessary for the preferentially-evaporating spray to start penetrating the flame, when compared to the non-preferential model.

The gas-phase axial velocity extrema at the start of the first reaction zone also serves as a reference flame speed in a twin-flame context [23], which we will adapt and refer to here as the *fuel consumption speed*. Additionally, because this velocity decreases from the point of injection to the stagnation plane, the fuel consumption speed is a useful way of characterizing the location of the first reaction zone, as well as the reaction rate at this point.

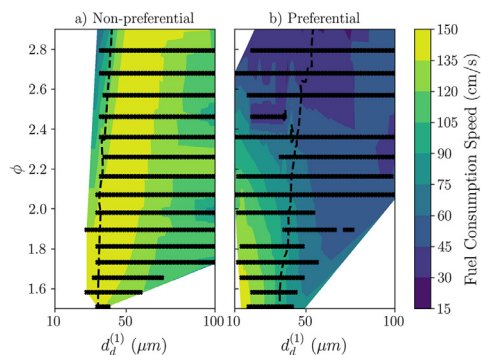


Fig. 6. Comparison of fuel consumption speed across varying  $\phi$  and  $d_d^{(1)}$  for (a) non-preferential and (b) preferential flames. The contour of zero penetration distance is indicated by a dashed line. Solution conditions are indicated with black symbols.

Here, the preferential and non-preferential flames seem to have a different dependence on the physical parameters, with the non-preferential flames having a consistent band of maximum speed which shifts to larger diameters with increasing  $\phi$ , while the preferential flames have decreasing speed with both variables. Additionally, the fuel consumption speed is consistently lower across this parameter space when preferential evaporation is considered.

Investigation of the flame structures across these varying parameters, as presented in Fig. 7, provides additional insight into this behavior. Here we see the change in flame structure with varying equivalence ratio, transitioning from a collocated flame [13] at rich conditions to approach a segregated structure as the equivalence ratio is lowered. This behavior is consistent for both preferential and non-preferential models, and we note that while the HTC region has a similar structure for both, the LTC region is significantly shifted. In the preferential cases, the LTC region occurs significantly further downstream, leading to the lower fuel consumption speeds seen in Fig. 6. Based on the fuel mass ratio  $Z_l = n_l m_l / \rho_g$ , we see that the majority of the droplet evaporation occurs upstream of any significant chemistry behavior, and that the evaporation behavior is therefore largely driven by the injection temperature of the gas phase. As expected from the zero-dimensional simulations, the droplets in the preferential cases extend significantly further downstream. These behaviors are highlighted when projecting these flames into the space of the gaseous mixture fraction

$$Z_g = \frac{W_F}{N_{C,F} W_C} \sum_k \frac{N_{C,k} W_C Y_{g,k}}{W_k}, \quad (5)$$

where  $W_k$  is the molecular weight and  $N_{C,k}$  is the number of carbon atoms in species  $k$ , as depicted in Fig. 8.

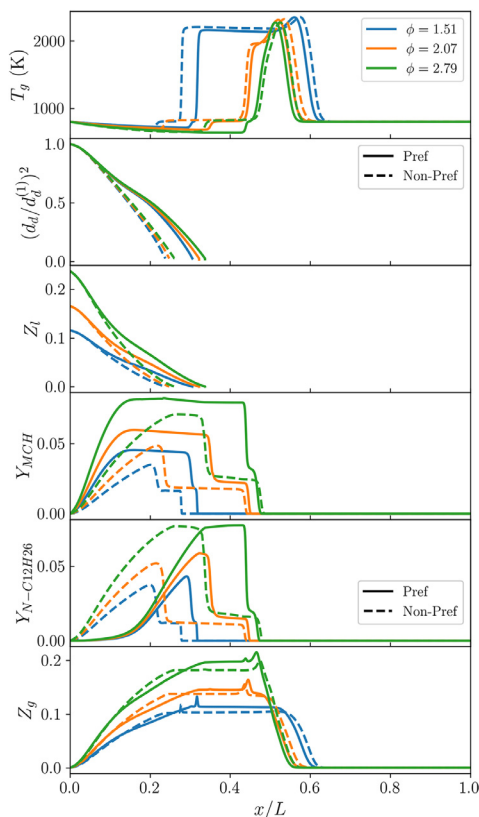


Fig. 7. Variation of flame structure with changing  $\phi$  for  $d_d^{(1)} = 38 \mu\text{m}$ , with both preferential and non-preferential evaporation models.

The profile of  $T_g$  in this space reveals the increasing significance of the partially-premixed flame, with a nearly vertical line indicating heat release at a constant mixture fraction for the case with  $\phi = 1.51$ . In each case, on the oxidizer inlet side, the behavior is similar for all cases; however, we see a shift in both low and high-temperature chemistry regions towards higher mixture fractions when preferential evaporation is considered. Again, it is clear that the majority of evaporation occurs prior to the LTC. The fuel mass ratio is consistently higher for the preferential cases. Finally, the change in gas-phase composition is highlighted as the preferential cases have significantly higher proportions of MCH and nearly no  $n$ -dodecane until the MCH is fully evaporated and plateaus.

Based on these results, it is clear that attempting to construct models of multicomponent spray combustion without accounting for preferential evaporation will yield significantly different results. For example, in a tabulated chemistry method [7], which relies on mixture fraction as a state space variable, the modeled temperature and composition profiles will not agree with the

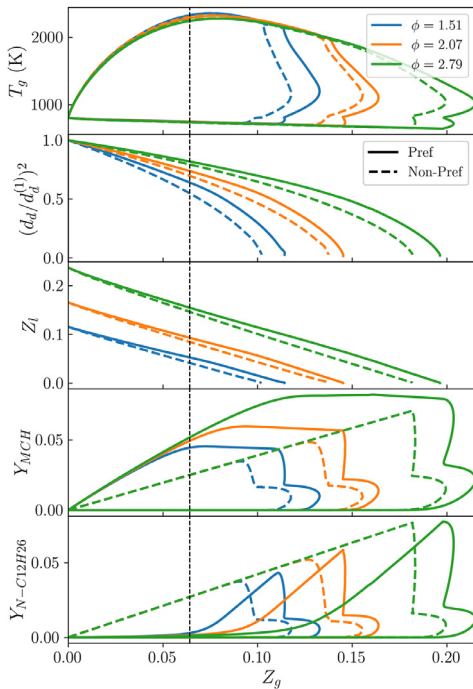


Fig. 8. Variation of flame structure with changing  $\phi$  for  $d_d^{(1)} = 38 \mu\text{m}$ , with both preferential and non-preferential evaporation models, plotted in the space of the mixture fraction,  $Z_g$ . The stoichiometric mixture fraction is indicated with a black dashed line.

detailed chemistry in the low-temperature and partially-premixed reaction zones.

## 5. Conclusions

This work studied the effect of preferential evaporation on laminar counterflow spray flames. Zero-dimensional simulations of droplet evaporation and one-dimensional simulations of spray flames were performed across a wide range of equivalence ratios and droplet diameters, using a 3-component surrogate fuel representation for Jet-A POSF 4658.

One-dimensional simulations across a wide range of operating conditions revealed large variations in flame structure and combustion chemistry. These simulations allowed the differences between non-preferential and preferential evaporation behavior to be characterized in terms of global parameters such as the distance of spray penetration into the flame structure, as well as the fuel consumption speed at the start of the first reaction zone. These global quantities display marked differences when preferential evaporation is considered: despite their longer droplet lifetimes, preferentially evaporating sprays penetrated the flame

structure significantly less than non-preferential sprays across the parameter space. Additionally, preferentially evaporating sprays featured a significantly lower fuel consumption speed that monotonically decreases with increasing equivalence ratio, compared to non-preferential sprays which, across equivalence ratios, feature a diameter at which fuel consumption speed is maximized.

Investigation into individual flame structures revealed the cause of these changes to be a shift in the location of the low-temperature chemistry zone in the flames with preferentially evaporating droplets. Consideration of the low-temperature chemistry revealed that the penetration distance of these preferential sprays is associated with a significant change in the gas-phase composition. The preferential model leads to significant evaporation of methylcyclohexane, the most volatile component, prior to the other components. Methylcyclohexane is far less reactive in the low temperature regime than *n*-dodecane, which is less volatile and remains in liquid phase until the end of the droplet's lifetime. This delays the low-temperature reaction zone until further downstream, resulting in lower fuel consumption speed. These results demonstrate the significant impact that multicomponent fuel evaporation has on the behavior of spray flames, especially concerning low-temperature chemistry. Therefore, in developing combustion models for multicomponent sprays, it is critical to consider these effects.

The simulations presented in this work are limited to monodisperse sprays, and the droplet diameters and strain rates are limited such that droplets do not cross the stagnation plane, which is not represented by this formulation. Extending these investigations to polydispersity, larger droplet diameters and varying strain rates, as well as alternative surrogate fuels, is the subject of future study.

## Declaration of Competing Interest

The authors declare that they have no known competing financial interests or personal relationships that could have appeared to influence the work reported in this paper.

## Acknowledgments

Financial support by the NASA Fellowship Activity program, training grant #80NSSC21K2054 and the Navy STTR program, contract #N68335-19-C-0177, is acknowledged.

## References

- [1] T. Edwards, *J. Propul. Power* 19 (6) (2012) 1089–1107, doi:[10.2514/2.6946](https://doi.org/10.2514/2.6946).
- [2] W.A. Sirignano, *Prog. Energy Combust. Sci.* 9 (4) (1983) 291–322, doi:[10.1016/0360-1285\(83\)90011-4](https://doi.org/10.1016/0360-1285(83)90011-4).



- [3] E. Gutheil, W.A. Sirignano, *Combust. Flame* 113 (1–2) (1998) 92–105, doi:[10.1016/S0010-2180\(97\)00192-2](https://doi.org/10.1016/S0010-2180(97)00192-2).
- [4] M. Colket, J. Heyne, *Fuel Effects on Operability of Aircraft Gas Turbine Combustors*, American Institute of Aeronautics and Astronautics, Inc., 2021.
- [5] E. Gutheil, Modeling and simulation of droplet and spray combustion (2010) 205–227, doi:[10.1002/9783527628148.boc009](https://doi.org/10.1002/9783527628148.boc009).
- [6] F. Bottone, A. Kronenburg, D. Gosman, A. Marquis, *Flow, Turbul. Combust.* 89 (4) (2012) 651–673, doi:[10.1007/S10494-012-9415-Y](https://doi.org/10.1007/S10494-012-9415-Y). 2012 894
- [7] B. Franzelli, A. Vié, M. Ihme, *Combust. Theory Model.* 19 (6) (2015) 773–806, doi:[10.1080/13647830.2015.1099740](https://doi.org/10.1080/13647830.2015.1099740).
- [8] S. Bhattacharjee, D.C. Haworth, *Combust. Flame* 160 (10) (2013) 2083–2102, doi:[10.1016/j.combustflame.2013.05.003](https://doi.org/10.1016/j.combustflame.2013.05.003).
- [9] C. Ji, E. Dames, Y.L. Wang, H. Wang, F.N. Egolfopoulos, *Combust. Flame* 157 (2) (2010) 277–287, doi:[10.1016/j.combustflame.2009.06.011](https://doi.org/10.1016/j.combustflame.2009.06.011).
- [10] J. Smolke, F. Carbone, F.N. Egolfopoulos, H. Wang, *Combust. Flame* 190 (2018) 65–73, doi:[10.1016/j.combustflame.2017.11.009](https://doi.org/10.1016/j.combustflame.2017.11.009).
- [11] G. Continillo, W.A. Sirignano, *Combust. Flame* 81 (3–4) (1990) 325–340, doi:[10.1016/0010-2180\(90\)90029-Q](https://doi.org/10.1016/0010-2180(90)90029-Q).
- [12] N. Darabiha, F. Lacas, J.C. Rolon, S. Candel, *Combust. Flame* 95 (3) (1993) 261–275, doi:[10.1016/0010-2180\(93\)90131-L](https://doi.org/10.1016/0010-2180(93)90131-L).
- [13] W. Xie, P.B. Govindaraju, Z. Ren, M. Ihme, *Proc. Combust. Inst.* 38 (2) (2021) 3193–3200, doi:[10.1016/j.proci.2020.06.274](https://doi.org/10.1016/j.proci.2020.06.274).
- [14] H. Olguin, E. Gutheil, *Combust. Flame* 161 (4) (2014) 987–996, doi:[10.1016/j.combustflame.2013.10.010](https://doi.org/10.1016/j.combustflame.2013.10.010).
- [15] H. Miyagawa, M. Nagaoka, K. Ohsawa, T. Yamada, *Jpn. Soc. Autom. Eng. Rev.* 19 (4) (1998) 299–304, doi:[10.1016/S0389-4304\(98\)00021-6](https://doi.org/10.1016/S0389-4304(98)00021-6).
- [16] W.A. Sirignano, G. Wu, *Int. J. Heat Mass Transf.* 51 (19–20) (2008) 4759–4774, doi:[10.1016/j.ijheatmasstransfer.2008.02.018](https://doi.org/10.1016/j.ijheatmasstransfer.2008.02.018).
- [17] T. Kitano, J. Nishio, R. Kurose, S. Komori, *Fuel* 136 (2014) 219–225, doi:[10.1016/j.fuel.2014.07.045](https://doi.org/10.1016/j.fuel.2014.07.045).
- [18] P.B. Govindaraju, M. Ihme, *Int. J. Heat Mass Transf.* 102 (2016) 833–845, doi:[10.1016/j.ijheatmasstransfer.2016.06.079](https://doi.org/10.1016/j.ijheatmasstransfer.2016.06.079).
- [19] A. Stagni, L. Esclapez, P. Govindaraju, A. Cuoci, T. Faravelli, M. Ihme, *Proc. Combust. Inst.* 36 (2) (2017) 2483–2491, doi:[10.1016/j.proci.2016.06.052](https://doi.org/10.1016/j.proci.2016.06.052).
- [20] P.B. Govindaraju, T. Jaravel, M. Ihme, *Proc. Combust. Inst.* 37 (3) (2019) 3295–3302, doi:[10.1016/j.proci.2018.05.166](https://doi.org/10.1016/j.proci.2018.05.166).
- [21] C. Wang, A.M. Dean, H. Zhu, R.J. Kee, *Combust. Flame* 160 (2) (2013) 265–275, doi:[10.1016/j.combustflame.2012.10.012](https://doi.org/10.1016/j.combustflame.2012.10.012).
- [22] V. Shastri, Q. Cazerres, B. Rochette, E. Riber, B. Cuenot, *Proc. Combust. Inst.* 38 (2) (2020) 3201–3211, doi:[10.1016/j.proci.2020.07.090](https://doi.org/10.1016/j.proci.2020.07.090).
- [23] L. Fan, B. Tian, C.T. Chong, M.N. Mohd Jaafar, K. Tanno, D. McGrath, P.M. de Oliveira, B. Rogg, S. Hochgreb, *Combust. Flame* 229 (2021) 111377, doi:[10.1016/j.combustflame.2021.02.023](https://doi.org/10.1016/j.combustflame.2021.02.023).
- [24] W.A. Sirignano, *Fluid Dynamics and Transport of Droplets and Sprays*, Cambridge University Press, 2010.
- [25] B. Franzelli, B. Fiorina, N. Darabiha, *Proc. Combust. Inst.* 34 (1) (2013) 1659–1666, doi:[10.1016/j.proci.2012.06.013](https://doi.org/10.1016/j.proci.2012.06.013).
- [26] R.S. Miller, K. Harstad, J. Bellan, *Int. J. Multiph. Flow* 24 (6) (1998) 1025–1055, doi:[10.1016/S0301-9322\(98\)00028-7](https://doi.org/10.1016/S0301-9322(98)00028-7).
- [27] S.K. Aggarwal, A.Y. Tong, W.A. Sirignano, *AIAA J.* 22 (10) (1984) 1448–1457, doi:[10.2514/3.8802](https://doi.org/10.2514/3.8802).
- [28] D.G. Goodwin, R.L. Speth, H.K. Moffat, B.W. Weber, Cantera: an object-oriented software toolkit for chemical kinetics, thermodynamics, and transport processes, 2021, (<https://www.cantera.org>). Version 2.5.1. doi:[10.5281/zenodo.4527812](https://doi.org/10.5281/zenodo.4527812).
- [29] K. Narayanaswamy, H. Pitsch, P. Pepiot, *Combust. Flame* 165 (2016) 288–309, doi:[10.1016/j.combustflame.2015.12.013](https://doi.org/10.1016/j.combustflame.2015.12.013).
- [30] P.J. Linstrom, NIST Chemistry WebBook, <http://webbook.nist.gov> (2005).
- [31] X. Fang, Z. Huang, X. Qiao, D. Ju, X. Bai, *Fuel* 229 (2018) 53–59, doi:[10.1016/j.fuel.2018.04.159](https://doi.org/10.1016/j.fuel.2018.04.159).
- [32] H.J. Curran, *Proc. Combust. Inst.* 37 (2019) 57–81, doi:[10.1016/j.proci.2018.06.054](https://doi.org/10.1016/j.proci.2018.06.054).
- [33] R. Yuan, J. Kariuki, E. Mastorakos, *Int. J. Spray Combust. Dyn.* 10 (3) (2018) 185–210, doi:[10.1177/1756827718763559](https://doi.org/10.1177/1756827718763559).